Protoplasma (1997) 198: 27–35

PROTOPLASMA

An NMR microscopic study of grape (*Vitis vinifera* L.)

S. M. Glidewell[1,*], B. Williamson[1], B. A. Goodman[1], J. A. Chudek[2], and G. Hunter[2]

[1] Scottish Crop Research Institute and [2] Department of Chemistry, Dundee University, Dundee

Received November 29, 1996
Accepted January 23, 1997

Summary. Mature healthy grape berries and berries wound-inoculated with the fungus *Botrytis cinerea* were examined by ^{1}H NMR microimaging using 2D and 3D spin echo and gradient echo procedures. These NMR images were compared with representations obtained by conventional histology, where possible using the same specimens. 3D imaging datasets from excised seeds were reconstructed by surface rendering and maximum intensity projection to allow interpretation of their internal structure. T_2-weighted spin echo images revealed the major features of the pericarp, septum and loculi of whole berries. T_1-weighted images were less discriminatory of parenchyma tissues in the fruit but revealed the endosperm in seeds as a chemically shifted feature. A non-invasive study by T_1-weighted spin echo NMR imaging of infection by *B. cinerea* over a 6-day period showed that the disease spread throughout the exocarp but failed to spread in the mesocarp, a result confirmed by histological examination of the same specimen. Surface rendering of 3D datasets of excised seeds revealed the two ruminations of the endosperm and the distal location of the chalaza. The position of the embryonic axis was revealed in T_2-weighted maximum intensity projections. This non-invasive study revealed the need to apply a range of imaging techniques and parameters to visualise the structural features of the different parts of the grape berry.

Keywords: *Botrytis cinerea*; *Vitis vinifera*; Embryonic axis; Endosperm; Fungal damage; Nuclear magnetic resonance imaging; Seed.

Abbrevations: BF bright field; FDA fluorescein diacetate; FI field inhomogeneity; FOV field of view; NMR nuclear magnetic resonance; RF radiofrequency; T_1 spin-lattice relaxation time; T_2 spin–spin relaxation time; TE echo time; TMS tetramethylsilane; TR repeat time.

*Correspondence and reprints: Scottish Crop Research Institute, Invergowrie, Dundee DD2 5DA, Scotland.

Introduction

Production of grapes (*Vitis vinifera* L.) for making wine, champagne, and cognac and also for use as dessert fruits and for juice extraction is important to the economy of many countries; seeds are also a valuable source of oil for culinary purposes. The structure and composition of the fruit are affected by genetic and environmental factors; the timeliness of harvest and presence of fungal pathogens, especially *Botrytis cinerea* Pers.: Fr., the cause of the deleterious bunch rot (Bulit and Dubos 1988) as well as the beneficial "noble rot" so important to the making of certain sweet wines (Ribéreau-Gayon et al. 1980), have a major impact on the value of the product. Knowledge of the changes which occur during growth, maturation, post-harvest storage, and fungal infection of the fruit is, therefore, essential to underpin these commercial endeavours.

Grapes are difficult specimens for conventional histological methods because of their high water content, large cell size, and, in many cultivars, hard seeds; nevertheless, considerable information is available from these sources about tissue differentiation and development (Harris et al. 1968, Considine and Knox 1979, Nii and Coombe 1983, Coombe 1987). While knowledge of the fluid phase of each cell type is important in viticulture and in the aetiology of disease processes, it cannot be derived by conventional histology; hence there is a reliance on destructive sampling and chemical analyses (e.g., Coombe 1987).

NMR microscopy allows the study of internal struc-

tures in grape through differences in the relaxation properties and/or chemical shifts of their fluid constituents and, because of its non-invasive nature, individual specimens can be characterised at various stages of their development. The technique has previously been used successfully in several studies of grape berries (Pope et al. 1991, 1992, 1993; Rumpel and Pope 1992; Goodman et al. 1993), where it has been demonstrated that both spin echo- and gradient echo-based pulse sequences can provide discrimination of the major tissue types.

We report here an extension of these investigations to include the use of 2D and 3D NMR imaging techniques to study the physical and chemical properties of the fluid phases in conjunction with conventional histology to validate the interpretation of the structural data. Procedures are described for discrimination of tissue damaged as a result of fungal infection and special attention is given to the study of seeds, both in intact berries and as separate entities.

Material and methods

Plant material and histology

Specimens were of the seeded grape (*Vitis vinifera* L.) cv. Black Hambourg glasshouse-grown near Dundee or other identified cultivars purchased from local supermarkets. Seeds were dissected from some ripe fruits and studied separately. Healthy fruits were harvested by cutting the pedicel c. 10 mm from the berry and the berry with pedicel attached was incubated at high humidity for the duration of the experiment.

To assess the contribution to the image of disease processes, specimens of grape cv. Thomson Seedless obtained from local supermarkets were locally surface-disinfected with 80% ethanol and wound-inoculated with conidia of *B.cinerea* isolate 448, originally obtained from raspberry, as described by Goodman et al. (1992). As wounded controls, other adjacent berries on the same bunch were also surface-disinfected and penetrated with a sterile needle. In this inoculation experiment fruits were incubated at high humidity for 48 h at room temperature before cutting the pedicel and mounting in the spectrometer. For histological examination of the same specimen after NMR microimaging, the berry was cut longitudinally by scalpel close to the mid-line in the plane of the needle wound, embedded in 3% distilled water agar and sliced longitudinally (c. 200 μm thick) using a Vibratome (752M Vibroslice; Campden Instruments Ltd., supplied by Micro Instruments Ltd., Long Hanborough, Oxon, U.K.). The sections were immersed in fluorescein diacetate (FDA) and examined by fluorescence microscopy with a Nikon confocal laser scanning microscope (in non-scanning mode) at 488 nm. The non-polar molecule of FDA is transported through the plasma membrane of live cells where an esterase cleaves off the acetate moiety leaving fluorescein to accumulate inside the cells which then fluoresce yellow-green when viewed by fluorescence microscopy. The same sections were then also examined by differential interference contrast microscopy with a Zeiss Universal Microscope.

NMR imaging

Whole berry specimens for NMR measurements were placed gently on a moist pad of cotton wool or supported on a section of plastic tubing in a 25 mm o.d. flat-bottomed sample tube, which was then inserted into the NMR imaging probe. Excised seeds were supported in plastic pipette tips over, but not in contact with, water to maintain humidity. "Stripped" seeds were generated by removal of the soft outer layers of the seed to leave only the hard layer containing the endosperm and the embryo. A series of 2D and 3D spin echo and gradient echo images were accumulated either as 256^2 matrices for 2D experiments or as $128\times128\times256$ or 128^3 matrices for 3D measurements using Bruker standard spin echo and gradient echo routines on Bruker AM300/WB or AMX300/SWB FT NMR spectrometers (7.1 T; ^{1}H, 300 MHz) fitted with microimaging probes with 25 mm coils for whole berries and 10 mm coils for excised seeds. Final spatial resolution was dependent on sample size but, except where stated otherwise, voxel sizes were: 2D $(100\ \mu m)^3$; 3D $(78\ \mu m)^3$. Other relevant acquisition data are presented in the legends to the figures.

After acquisition, data were transformed using sine or Qsine bell weighting on Bruker X32 computers, Unix-based systems which incorporate the Bruker UXNMR suite of programs and then processed to give single slice, multislice and 3D datasets. Surface reconstructions were also performed when considered appropriate for enhancing the extraction of information from 3D images (see Williamson et al. 1994).

Signal intensity in NMR images

The contrast between different tissue types was found to depend not only on the type of imaging sequence, e.g., spin echo or gradient echo, and the weighting used, i.e., T_1, T_2, or none, but also on the shape of the soft radiofrequency (RF) pulse. For details, see standard NMR texts (e.g., Callaghan 1991), but a brief description is as follows.

In an NMR experiment, the sample is placed in a strong magnetic field which causes atomic nuclei which have a magnetic moment (e.g., ^{1}H), to align with the applied magnetic field and precess about it; this precessional frequency is normally in the radiofrequency range.

When an appropriate pulse of radiofrequency energy (RF) at this precessional frequency is applied, the nuclei resonate: the magnetisation is inverted and the nuclei precess in phase with one another. When the RF ceases, the nuclei relax back to their equilibrium state in which they are aligned with the applied magnetic field and they start to lose phase coherence. The former process is called longitudinal or spin-lattice relaxation and occurs at a rate $(T_1)^{-1}$. The latter dephasing process is called transverse or spin–spin relaxation, described by a relaxation rate $(T_2)^{-1}$. Not all nuclei of a given element resonate at precisely the same frequency: differences in the surrounding electron density lead to differences in the effective magnetic field at the nucleus. Such shifts in the resonant frequency are called chemical shifts and are of the order of a few parts per million for protons. Larger shifts in resonant frequency can also be induced by varying the applied magnetic field: the magnetic field and resonant frequency for any nucleus are proportional to one another. The application of orthogonal linear magnetic field gradients across a sample and the use of a spectrum of RF frequencies thus allow the spatial origin of a signal to be deduced. By selectively exciting a particular slice of a sample, an image of that slice may be reconstructed.

The NMR signal which gives rise to the image is derived from an echo. In a spin echo experiment, a hard RF pulse (i.e., a short pulse

which excites all the protons) tips the magnetisation through 90°. After a time TE/2, during which both T_1 and T_2 processes occur, a second slice-selective soft RF pulse (i.e., a relatively long pulse at lower intensity) is applied to refocus the magnetisation as an echo at time TE which is then detected. A gradient echo experiment uses reversal of the magnetic field gradients to form the echo and uses only a soft RF pulse. In 3D spin echo experiments, the soft slice-selective pulse is replaced by a hard refocusing pulse. To obtain optimal results, the soft pulses are usually modulated to give a shaped pulse: common shapes used are sinc or hermite.

In spin echo images, contrast arises from differences across the sample in the true transverse or spin–spin relaxation time, T_2, and signal intensity is proportional to $\exp(-TE/T_2)$. In gradient echo images, contrast arises from differences across the sample in the actual transverse relaxation time, T_2^*, and signal intensity is proportional to $\exp(-TE/T_2^*)$. These two terms are related by the equation:

$$(T_2^*)^{-1} = (T_2)^{-1} + (T_{2FI})^{-1}$$

where in a given voxel $(T_2^*)^{-1}$ is the observed rate of spin dephasing in the absence of RF refocusing, $(T_2)^{-1}$ the rate of spin dephasing due to true T_2, $(T_{2FI})^{-1}$ the rate of dephasing due to magnetic field inhomogeneity.

T_1 (or spin-lattice relaxation time) contrast effects are the result of signal attenuation due to saturation if the repetition time, TR, is insufficiently long ($TR < 5T_1$). Signal intensity in a given voxel increases as TR is increased and then reaches a plateau at $TR \geq 5T_1$. T_1 is much less likely to be affected by field inhomogeneities than is the spin–spin relaxation time. T_1-weighted images are generated by using short TRs: only those areas with short T_1s will have relaxed back to equilibrium before the next excitation pulse and they will have the highest intensities. T_2-weighted images show high intensity in areas with long T_2s: in areas with short T_2s, the signal has lost phase coherence before the refocusing pulse.

Results and discussion

Proton spectra of intact fruit consist of a major peak at 4.6 ppm with minor resonances at 3.4 and 1.1 ppm relative to tetramethylsilane (TMS); total ^1H and chemical shift selective 2D images have been reported previously (Pope et al. 1991, 1992, 1993; Rumpel and Pope 1992; Goodman et al. 1993). These images revealed considerable structural detail in the parenchyma tissue of the pericarp, although seeds often appeared as dark featureless entities, except in chemical shift selective images based on the 1.1 ppm resonance. Similar measurements will be considered briefly here in order to place the present measurements in a proper context. 2D images of the resonance at 1.1 ppm resemble a cross-section of the endosperm (e.g., Pope et al. 1991), which represents the major source of lipids in the seeds. The 3.4 ppm peak may contain contributions from magnetic susceptibility induced shifts to part of the water resonance, as well as from low molecular weight sugar molecules in solution in the pericarp.

Image dependence on NMR parameters

A comparison in Fig. 1 of T_1-and T_2-weighted images of the same specimen for spin and gradient echo shows that spin echo images produced greater tissue contrast as TE increased than did gradient echo images, thus indicating that $(T_{2FI})^{-1} \gg (T_2)^{-1}$. The spin echo images have fewer artefacts around the seeds which is consistent with the known sensitivity of gradient echo images to discontinuities in magnetic susceptibility, $\chi_m = (M_0/B_0 - 1)$ where M_0 is the induced magnetisation and B_0 the applied magnetic field (Callaghan 1991). Such discontinuities occur at the interfaces between different physical states of a specimen, e.g., gas spaces or embedded solids such as seeds. In the parenchymal tissue in both spin and gradient echo images there is appreciable signal intensity at a TR of 200 ms (Fig. 1 a, b), hence there must be substantial relaxation at this TR, indicating a T_1 value probably less than 150 ms, and, since $TR > 5T_1$ (see Material and methods) complete spin-lattice relaxation at TR = 2000 ms (Fig. 1 c, d). In spin echo images (Fig. 1 b, d) contrast increased as TE was increased from 10 to 100 ms indicating that there are

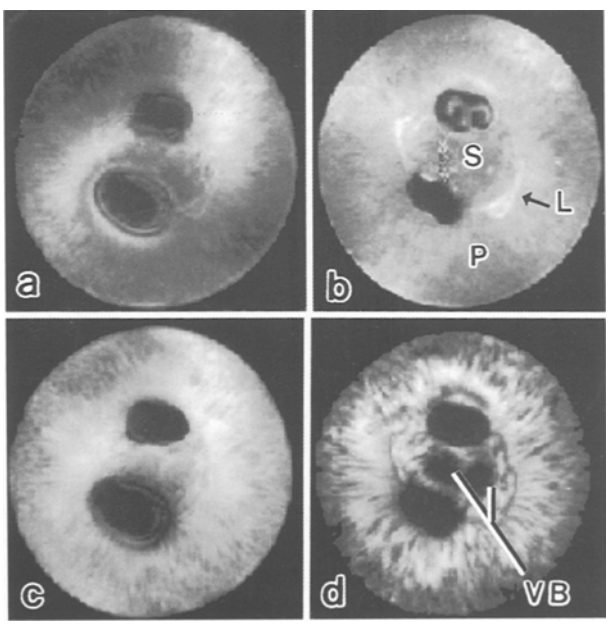

Fig. 1. T_1-weighted (**a** and **b**) and T_2-weighted (**c** and **d**) total ^1H gradient echo (**a** and **c**) and spin echo (**b** and **d**) images of a ripe grape berry cv. Black Hambourg in a median transverse plane with 25 mm FOV. Voxel dimensions, $(100\ \mu m)^3$; 180° pulse 78 μs; 90° sinc pulse 2000 μs; a and b: TE, 10 ms, TR, 200 ms; c and d: TE, 100 ms, TR, 2000 ms. *L* Locular cavity; *P* pericarp; *S* septum; *VB* vascular bundles

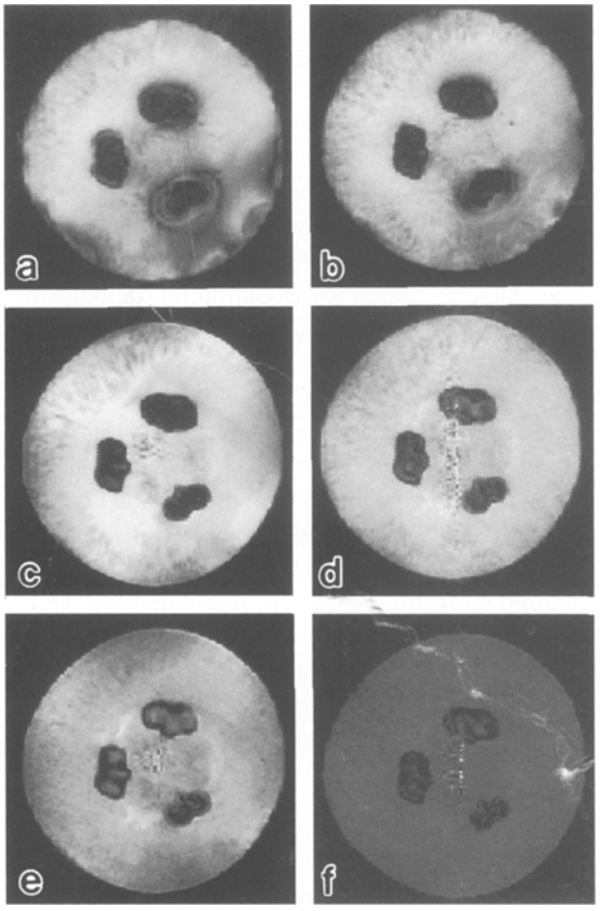

Fig. 2. Unweighted gradient echo (**a** and **b**) and spin echo (**c** and **d**) and T_1-weighted spin echo (**e** and **f**) images of a ripe grape berry cv. Black Hambourg in a median transverse plane with 25 mm FOV. (The vertical feature seen in **d** and **f** and less markedly in **c** and **e** is an imaging artefact caused by mains ripple.) Voxel dimensions $(100\ \mu m)^3$; 180° pulse 86 μs; a, c and e: 90° pulse 2000 μs (sinc); b, d and f: 4000 μs (hermite); a, b, and d: TE, 14 ms, TR, 1020 ms; c: TE, 18 ms, TR, 1020 ms; e and f: TE, 10 ms, TR, 200 ms

at least two quite different T_2 values – one short (significantly less than 20 ms) and the other much longer (greater than 40 ms). In gradient echo images (Fig. 1 a, c) there was very little increase in contrast on going from a TE of 10 to one of 100 ms, indicating that the rate of dephasing was controlled very largely by $(T_{2FI})^{-1}$. In spin echo images of whole grape berries (Fig. 1 b, d), the seeds showed internal contrast at a TE of 10 ms but not at 100 ms, indicating a short T_2, probably less than 10 ms. In gradient echo images (Fig. 1 a, c), there was no contrast at any value of TE, indicating that T_2^* is very short and probably less than 3 ms.

The effect of the shape of the soft RF pulse on the image is illustrated in Fig. 2, which compares images obtained with both gradient echo and spin echo sequences using sinc or hermite shaped pulses. The hermite pulse gives a less artefactual gradient echo image (Fig. 2 a, b) but considerably lower intensity than the sinc pulse in a T_1-weighted spin echo sequence (Fig. 2 e, f).

Structural features revealed in NMR images

In the median transverse plane, the locular cavity is compressed laterally by the expansion of the septum in the centre and the pericarp. The locular cavity therefore appears as a crescent-shaped feature in both spin and gradient-echo images (light in Fig. 1 b, dark in Figs. 1 d and 3). Bright field microscopy in 1.5 μm thick sections of resin-embedded immature grapes (Fig. 4) shows the relative sizes and orientation of cells in the compressed loculus. The endocarp lines the loculus and consists of an inner epidermis and a hypodermis of 2–3 cell layers occluded by prominent druses, intracellular crystals of calcium oxalate (Considine and Knox 1979, Webb et al. 1995) which were revealed by differential interference contrast microscopy (not shown). Prominent radially arranged striations seen in T_2-weighted spin echo images (e.g., Fig. 1 d) probably correspond to the distribution and alignment of panels of cells in the inner mesocarp which alternate in size (Fig. 4). Similar NMR images have been published by Pope et al. (1993). In transverse planal views (Fig. 1 d), dark entities in the centre of the septum represent the ventral bundles which

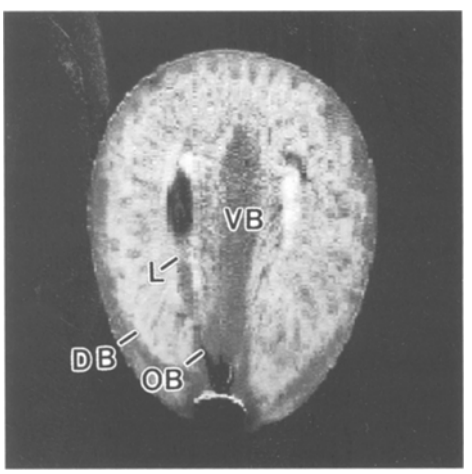

Fig. 3. Spin echo image with slight T_2-weighting of mature grape berry cv. Black Hambourg, median longitudinal view; TE, 18.3 ms; TR, 1020 ms; 90° pulse 52 μs, 180° hermite pulse 3000 μs; pixel size, $(117\ \mu m)^3$; slice thickness, 250 μm. *DB* Dorsal bundle network; *VB* ventral vascular bundle; *OB* ovular bundle; *L* loculus

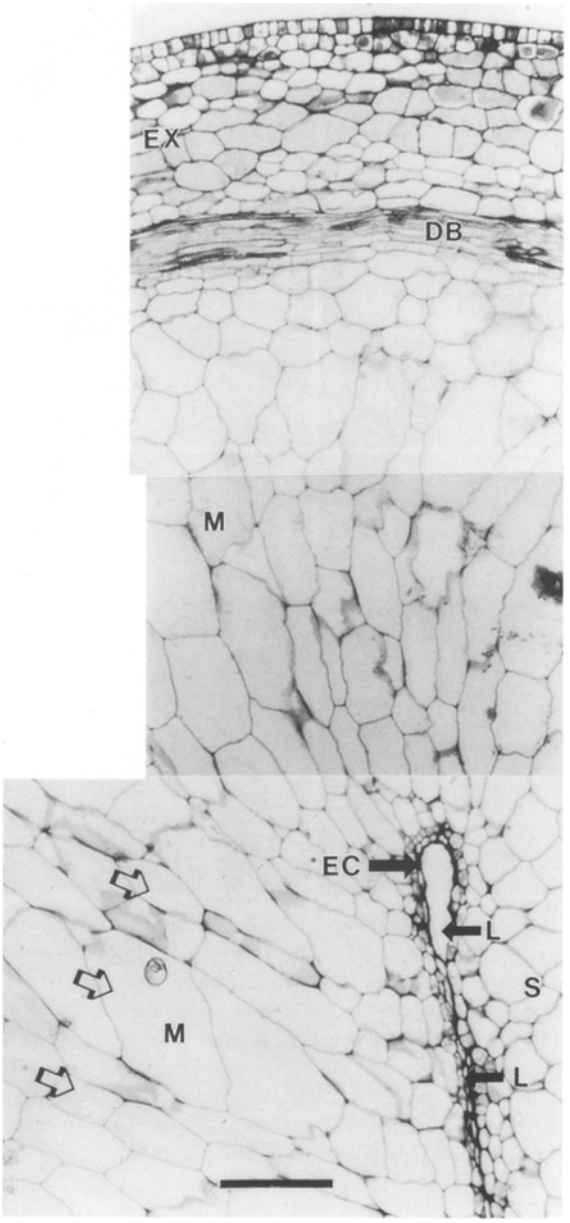

Fig. 4. Portion of developing Black Hambourg grape in median transverse section, stained by toluidine blue, viewed by bright field light microscopy showing arrangement of the tissues around a collapsed loculus (*L*) lacking a seed. The loculus is surrounded by the inner epidermis or endocarp (*EC*), with the central swollen septum (*S*), the mesocarp (*M*), and peripheral exocarp (*EX*). Radially elongated parenchyma cells of the mesocarp are packed in groups of small cells alternating with larger ones (outline arrows). The exocarp consists of 10–12 cell layers outside the dorsal bundle network (*DB*) (longitudinal view) at the boundary between mesocarp and exocarp (Coombe 1987). Bar: 100 μm

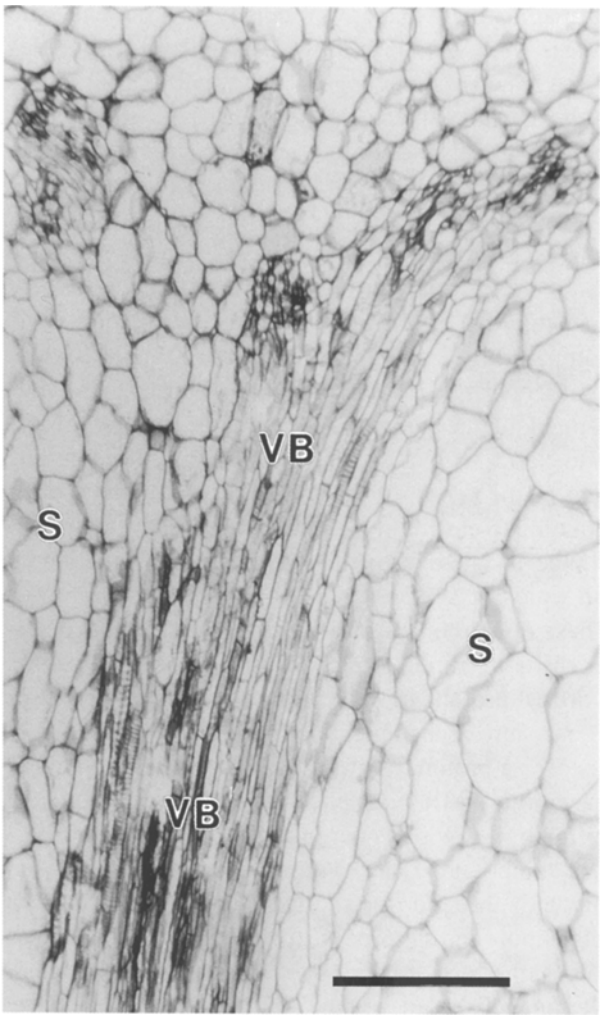

Fig. 5. The ventral vascular bundles (*VB*) within the septum (*S*) of Black Hambourg grape in median longitudinal section. The ventral bundles separate into smaller bundles at the distal end of the berry. Stained by toluidine blue and viewed by bright field light microscopy. Bar: 100 μm

are also clearly visible in median longitudinal views (Fig. 3) as dark strands. The ventral bundles (usually two) containing xylem and phloem tissues (Fig. 5), supply nutrients to the developing style of the carpel and distal regions of the pericarp. The vascular supplies to the seeds, the ovular bundles, are shown as prominent dark strands (Fig. 3) (Coombe 1987) at the proximal end of the berry and peripheral dark features correspond to the dorsal bundle network.

Internal structure in the seeds is revealed in spin echo images and is particularly pronounced when there is appreciable T_1 weighting (Figs. 1 b and 2 e). The bright mushroom-shaped features seen in one of the seeds in Fig. 1 b and two of the seeds in Fig. 2 correspond to the endosperm. The seeds in Figs. 1 b and 2 c–f, which appear dark in the centre were shown on subsequent sectioning to have no endosperm. These empty seeds also showed marked concentric rings of

alternating high and low intensity in gradient echo images, very similar to those arising from air bubbles in mayonnaise and agar gels (our unpubl. results); this is consistent with the greater sensitivity of gradient echo images to discontinuities in magnetic susceptibility (Pope et al. 1992). Gradient echo images of overripe grape berries also show such artefacts as well as loss of intensity, in areas near the surface which correspond to observed soft patches where there may be air pockets under the wrinkled "skin" (compare Fig. 2 a, b to Fig. 2 c–f).

Total ^{1}H NMR microscopy of many berries with seeds resulted in the generation of double images of the endosperm with a spatial separation shifted to the right of the centre of the image by an amount corresponding to ca. 3.9 ppm. This approximates to the difference in chemical shift between water at 4.6 ppm and lipids at 1.1 ppm relative to TMS (see above). (These double images arise from the different chemical shifts of aliphatic protons in lipid molecules and hydroxyl protons in water and solutes. Chemical shift is a measure of the magnetic shielding of a nucleus, in this case a proton, by the electrons in a molecule and causes the NMR resonance to occur at a frequency shifted by a few parts per million from that of a reference compound, TMS.) These images are thus consistent with the endosperm signal being derived from both lipid and hydroxyl (principally water) resonances, the former being seen in chemical shift selective images based on the 1.1 ppm resonance. The NMR microimaging method thus provides a procedure for the non-invasive study of the deposition of lipids in the endosperm of the seeds.

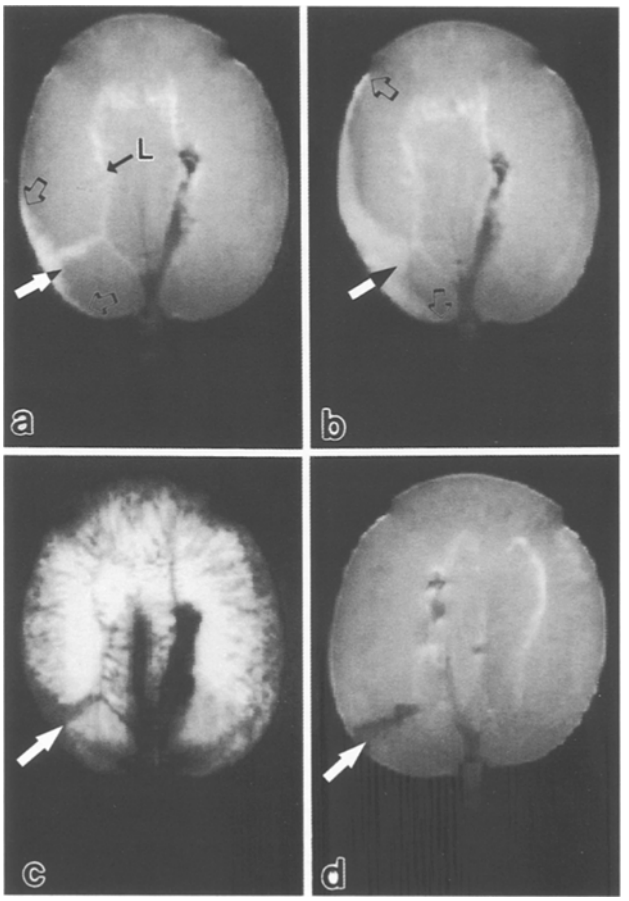

Fig. 6. Moderately T_1-weighted spin echo images of grape berry cv. Thomson Seedless inoculated with the fungal pathogen *Botrytis cinerea* obtained **a** 72 h and **b** 137 h after inoculation (TE, 10 ms; TR, 500 ms); **c** T_2-weighted image of same grape 90 h after inoculation (TE, 120 ms; TR, 1500 ms); **d** moderately T_1-weighted spin echo image of control grape 144 h after wounding (TE, 10 ms; TR, 500 ms); a–d: 180° pulse 70 μs, 90° sinc pulse 2000 μs; slice thickness, 50 μm; a–c: pixel size, (137 μm)^2, d: (117 μm). Arrow, point of needle entry; outline arrows, extent of disease; *L* loculus

Identification of fungally infected tissue

The needle track through the pericarp is visible in moderately T_1-weighted spin-echo images of inoculated berries as a bright sector penetrating as deep as the collapsed loculus (Fig. 6 a, b). A bright featureless area attributed to disease processes extended gradually over a 6-day period to affect the exodermis over approximately a third of the grape surface, but the mesocarp retained the appearance of the images of the healthy berry although some shrinkage in size is visible. A T_2-weighted spin echo image (Fig. 6 c) of the same grape shows the diseased tissue as dark. Figure 6 d shows a moderately T_1-weighted image of a control grape 5 1/2 days after wounding: the track of the needle is clearly visible but is dark in contrast to infected tissue imaged under the same conditions (Fig. 6 b) which may be a consequence of mechanical damage or may simply result from the fact that the needle left a hole in the tissue.

The dark spots at the edges of the fruit in this image correspond to pressure points where the grape sat on a section of plastic tubing; these appear as slight indentations in the images (Fig. 6), although no such indentations were visible on the grape after imaging.

After completing the imaging measurements, histological examination showed that the entire exodermis (all parenchyma tissues, hypodermis, and epidermis outside the dorsal bundle network, see Fig. 4) was ramified by fungal hyphae which fluoresced brightly in FDA. In the relatively thick slices, a high propor-

tion of the uninfected mesocarp cells also stained brightly. In contrast, the host cells adjacent to the needle track were unstained. Two ungerminated viable conidia were located amongst these dead host cells along the needle track within the mesocarp. By differential interference contrast microscopy, groups of ungerminated dead cells were visible in this area and the associated host cells were brown. These data support the non-invasive imaging data and suggest that host defence processes operate against *B. cinerea* most effectively in the mesocarp, and to a lesser extent in the exocarp.

Excised seeds from ripe fruit

Differences in contrast were observed between the endosperm and testa in different specimens over a wide range of T_1 and T_2 weightings, but in all cases the size and shape of the endosperm were consistently reproduced. The endosperm in *Vitis vinifera* is "ruminate" with two pronounced invaginations or folds (Corner 1976), one on either side of the raphe, to give a mushroom-shaped structure in median transverse planes.

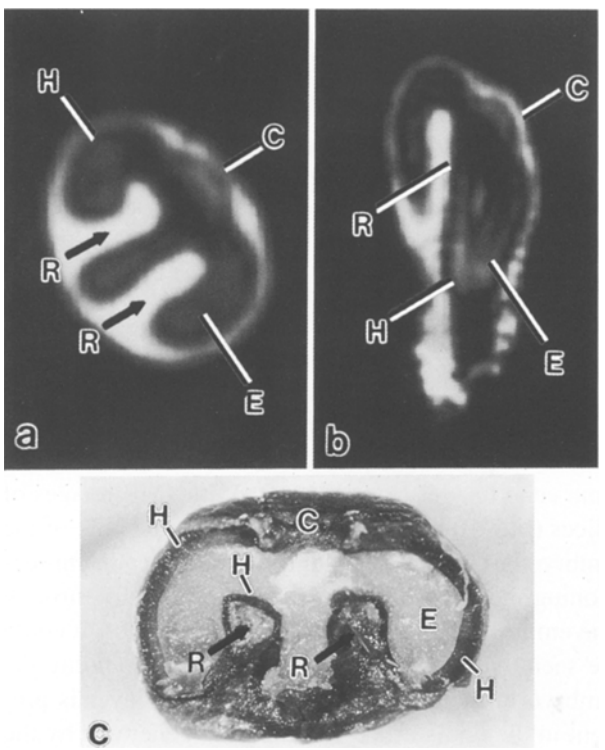

Fig. 7. Slices from a 3D spin echo dataset of a Black Hambourg seed: **a** transverse and **b** longitudinal view along with **c** photograph of a seed cut in a transverse plane. TE, 8.27 ms; TR, 1020 ms; 90° pulse 52 μs, 180° pulse 104 μs; voxel size, $(78\ \mu m)^3$. *C* Chalaza; *R* ruminations; *H* hard layer; *E* endosperm

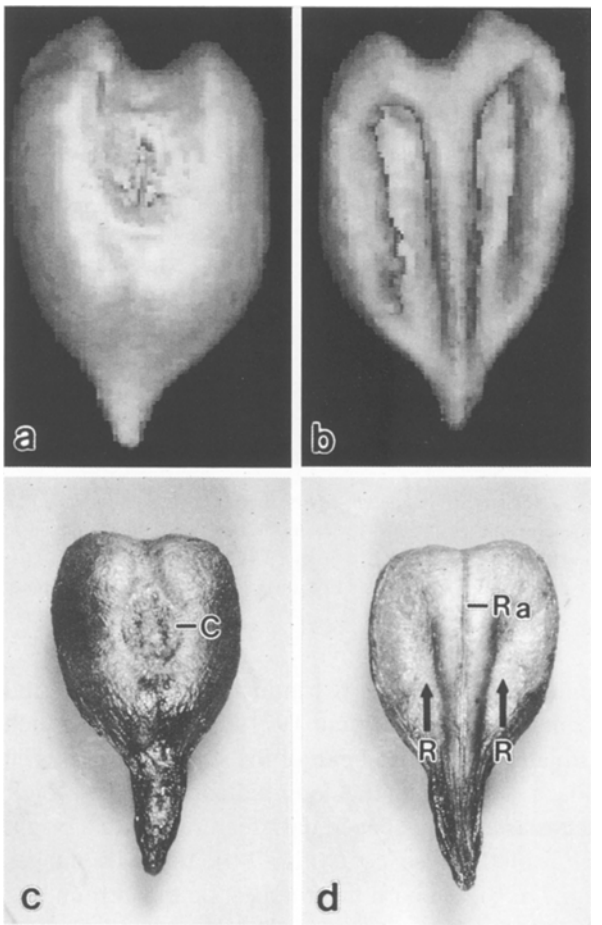

Fig. 8. a and **b** 3D surface-rendered images of the total proton spin echo signal associated with the endosperm in excised seeds of grape (cv. Italia) (TE, 6.56 ms; TR, 1000 ms; 90° pulse 16 μs, 180° pulse 32 μs; voxel size $(78\ \mu m)^3$). **c** and **d** Photographs of typical grape seeds; chalaza (*C*), raphe (*Ra*), rumination (*R*)

The testa, derived from the original two integuments enveloping the ovule, has at least four tissue layers in the mature seed (Fig. 7 c): an outer epidermis covered with an impervious lipid cuticle; parenchyma cells containing raphides (needle-like crystals) and phenolic material; the hard layer; and an inner epidermis (Vaughan 1970). The hard layer (Pratt 1971) [also described as the "mechanical tissue" (Periasamy 1962) or "elongated pitted stone cells" (Vaughan 1970)], represents the inner layer of the outer integument and consists of tightly packed thick-walled sclerenchymatous cells up to 20 μm in tangential diameter and up to 1 mm in radial diameter (Vaughan 1970). This hard layer varies in thickness in different positions around the endosperm, the layer being

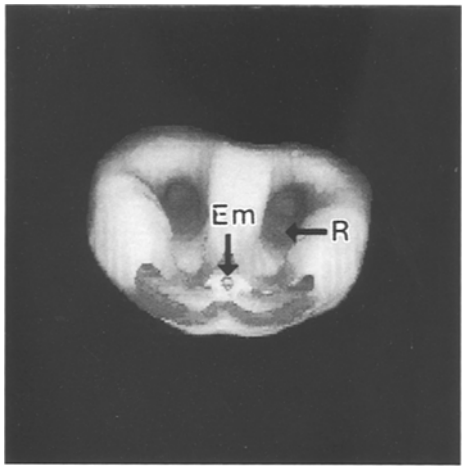

Fig. 9. 3D surface rendered unweighted spin echo image of the endosperm in a grape seed (cv. Red Globe) electronically sliced to reveal internal structure. TE, 6.56 ms; TR, 1500 ms; 90° pulse 12 μs, 180° pulse 24 μs; voxel size, $(117\ \mu m)^3$. *R* Rumination; *Em* embryo

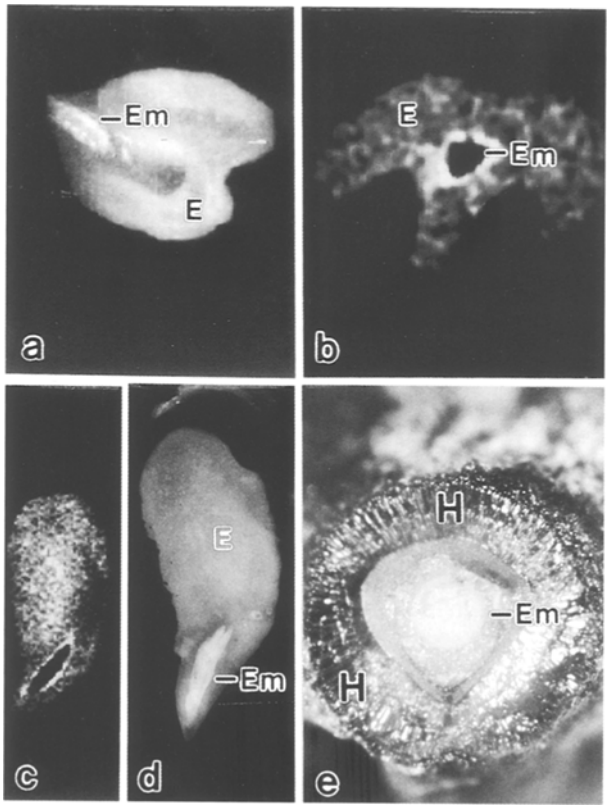

Fig. 10. a Maximum intensity projection, **b** transverse slice, **c** longitudinal slice of T_2-weighted 3D spin echo images of excised, "stripped" seeds of grape cv. Black Napoleon. (Voxel dimensions $(39\ \mu m)^3$; a: TE, 30 ms; TR, 1750 ms; 90° pulse 16 μs, 180° pulse 32 μs; b and c: TE, 35 ms, TR, 1000 ms; 90° pulse 19 μs, 180° pulse 38 μs.) Photographs of **d** longitudinally and **e** transversely bisected seed stained with 1% toluidine blue showing embryo (*Em*), endosperm (*E*), and hard layer (*H*)

thinnest within the two ruminations (Fig. 7 c) and absent at the chalaza (Pratt 1971, Corner 1976) which is situated at the distal end of the seed (Fig. 8 c). The chalaza appears in the longitudinal plane in NMR images as a dome-shaped dark feature within a bright region of the seed coat (Fig. 7 b). In NMR images (Fig. 7 a, b), the hard layer appears dark surrounding the endosperm, as it has no mobile protons, and the bright layer around this, and particularly within the ruminations, corresponds to the parenchyma cells of the testa (the exo-testa; Vaughan 1970). The endosperm appears darker relative to the testa parenchyma in these images in contrast to those in Figs. 1 b and 2 b, e which were obtained under slightly different conditions. The slices in Fig. 7 b are derived from a 3D dataset using two hard pulses whereas those in Figs. 1 b and 2 b, e are 2D images acquired using a soft and a hard pulse (see Material and methods).

In surface-rendered 3D-reconstructions of the endosperm (Figs. 8 b and 9), it is possible to discern clearly the ruminations which run longitudinally and terminate at the distal end as a pair of dark circular depressions (Fig. 9); such NMR images show a close resemblance to the external appearance of the hard layer of the seed. The internal shape of the endosperm is revealed more clearly by electronically cutting and reorienting this surface-rendered 3D image (Fig. 9). The image in Fig. 9 is similar to that reported by Pope et al. (1991) for a 2D chemical shift selective image of the 1.1 ppm resonance in the intact fruit. NMR images of transverse slices through seeds (e.g., Fig. 7 a) show the endosperm as a mushroom shape which is often shifted to the right (see above).

The embryonic axis is delineated as a bright feature in maximum intensity projections of 3D T_2-weighted spin echo images (e.g., Fig. 10 a). In NMR images of slices (Fig. 10 b, c), it can be seen that the bulk of the embryo is dark surrounded by a bright sheath. On sectioning the seeds with a blade longitudinally through the embryonic axis after imaging (Fig. 10 d), it could be seen that there was a liquid layer surrounding the embryo in the endosperm; if this liquid layer is present in the undisturbed seed and not generated by the mechanical disruption of sectioning, it would be expected to have a greater T_2 than the surrounding endosperm tissue, and thus give rise to the bright sheath in T_2-weighted images. T_1-weighted images of seeds also showed the embryo as dark, suggesting

therefore, that it has a short T_2 and a long T_1. This is in contrast to T_1-weighted NMR images observed for avocado seed (Goodman and Glidewell 1995), barley and rice (unpubl. obs.) in which the embryo shows greatly enhanced intensity relative to the endosperm.

Acknowledgements

We thank the Scottish Office Agriculture, Environment and Fisheries Department for funding and Mylnefield Research Services Ltd for providing the AMX300/SWB NMR facility. We thank Dr. D. J. F. Brown and Mr. B. Robertson for the donation of Black Hambourg grapes. We are grateful to Mr. D. Prior for suggestions and assistance in the use of the confocal laser scanning microscope to observe fungal infections in sliced grape tissue.

References

Bulit J, Dubos B (1988) *Botrytis* bunch rot and blight. In: Pearson RC, Goheen AC (eds) Compendium of grape diseases. APS Press, St Paul, MN, pp 13–15

Callaghan PT (1991) Principles of nuclear magnetic resonance microscopy. Oxford University Press, Oxford

Considine JA, Knox RB (1979) Development and histochemistry of the cells, cell walls, and cuticle of the dermal systems of the fruit of the grape, *Vitis vinifera*. Protoplasma 99: 347–365

Coombe BG (1987) Distribution of solutes within developing grape berry in relation to its morpholgy. Am J Enol Vitic 38: 120–127

Corner EJH (1976) The seeds of dicotyledons, vol I. Cambridge University Press, Cambridge

Goodman BA, Glidewell SM (1995) High field NMR microscopy of agricultural produce. Microsc Anal 50: 7–9

– McPhail DB, Duthie DML (1989) Electron spin resonance spectroscopy of some irradiated foodstuffs. J Sci Food Agric 47: 101–111

– Williamson B, Chudek JA (1992) Non-invasive observation of the development of fungal infection in fruit. Protoplasma 166: 107–109

– – – (1993) Identification of the distribution of sugars in grapes using chemical shift selective NMR microscopy. Magn Reson Imaging 11: 1039–1041

Harris JM, Kriedemann PE, Possingham J (1968) Anatomical aspects of grape berry development. Vitis 7: 106–119

Nii N, Coombe BG (1983) Structure and development of the berry and pedicel of the grape, *Vitis vinifera* L. Acta Hortic 139: 129–140

Periasamy K (1962) Studies on seeds with ruminate endosperm. II. Development of rumination in the Vitaceae. Proc Ind Acad Sci B 56: 13–26

Pope JM, Rumpel H, Kuhn W, Walker R, Leach D, Sarafis V (1991) Applications of chemical shift selective NMR microscopy to the noninvasive histochemistry of plant materials. Magn Reson Imaging 9: 357–363

– Walker RR, Kron T (1992) Artifacts in chemical shift selective imaging. Magn Reson Imaging 10: 695–698

– Jonas D, Walker RR (1993) Applications of NMR micro-imaging to the study of water, lipid, and carbohydrate distribution in grape berries. Protoplasma 173: 177–186

Pratt C (1971) Reproductive anatomy in cultivated grapes: a review. Am J Enol Vitic 22: 92–109

Rumpel H, Pope JM (1992) The application of 3D chemical shift microscopy to non-invasive histochemistry. Magn Reson Imaging 10: 187–194

Ribéreau-Gayon J, Ribéreau-Gayon P, Seguin G (1980) *Botrytis cinerea* in enology. In: Coley-Smith JR, Verhoeff K, Javis WR (eds) The biology of *Botrytis*. Academic Press, London, pp 251–274

Snowdon AL (1990) A colour atlas of post-harvest diseases and disorders of fruits and vegetables, vol 1, general introduction and fruits. Wolfe Scientific, London

Vaughan JG (1970) The structure and utilization of oil seeds. Chapman and Hall, London

Webb MA, Cavaletto JM, Carpita NC, Lopez LE, Arnott HJ (1995) The intravacuolar organic matrix associated with calcium oxalate crystals in leaves of *Vitis*. Plant J 7: 633–648

Williamson B, Goodman BA, Chudek JA, Hunter G, Lohman JAB (1994) The vascular architecture of the fruit receptacle of red raspberry determined by 3D NMR microscopy and surface-rendering techniques. New Phytol 128: 39–44